



Impact-Resilient Orchestrated Robust Controller for Heavy-Duty Hydraulic Manipulators

Mahdi Hejrati  and Jouni Mattila 

Abstract—Heavy-duty operations, typically performed using heavy-duty hydraulic manipulators (HHMs), are susceptible to environmental contact due to tracking errors or sudden environmental changes. Therefore, in addition to precise control, it is essential for the manipulator to maintain stability and reduce the risk of damage to both itself and the environment during contact, without relying on contact-force sensors, which are typically impractical for these applications. This article proposes a novel force-sensorless robust impact-resilient controller for a generic 6-degree-of-freedom (DoF) HHM constituting from anthropomorphic arm and spherical wrist mechanisms. The scheme consists of a neuroadaptive subsystem-based impedance controller, which is designed to ensure both accurate tracking of position and orientation with stabilization of HHMs upon contact, along with a novel generalized momentum observer, which is for the first time introduced in Plücker coordinate, to estimate the impact force. Finally, by leveraging the concepts of virtual stability and virtual power flow, the semiglobal uniformly ultimately boundedness of the entire system is assured. Extensive experiments and simulation comparisons conducted on a generic 6-DoF industrial HHM validate the method's exceptional performance in achieving subcentimeter accuracy for desired trajectory tracking. Furthermore, the results demonstrate that equipping the controller with impact-resiliency features reduces the impact force from unintended contacts by 80% .

Index Terms—Adaptive neural network, contact force estimation, hydraulic systems, impedance control.

I. INTRODUCTION

HYDRAULICALLY driven manipulators are extensively used in industrial applications, such as off-road mobile machines and heavy-duty operations, due to their distinct advantages, including a favorable size-to-power ratio and the ability to generate substantial output force or torque compared to their electrical counterparts [1], [2], [3], [4]. However, despite these

Received 16 August 2024; revised 26 November 2024 and 26 February 2025; accepted 12 April 2025. Recommended by Technical Editor S. Jeong and Senior Editor X. Chen. This work was supported by Business Finland partnership project "Future all-electric rough terrain autonomous mobile manipulators" under Grant 2334/31/222. (Corresponding author: Mahdi Hejrati.)

The authors are with the Department of Engineering and Natural Science, Tampere University, 7320 Tampere, Finland (e-mail: mahdi.hejrati@tuni.fi; jouni.mattila@tuni.fi).

This article has supplementary material provided by the authors and color versions of one or more figures available at <https://doi.org/10.1109/TMECH.2025.3562394>.

Digital Object Identifier 10.1109/TMECH.2025.3562394

benefits, the design of a stable, high-precision controller for hydraulic actuators is challenging due to the governing non-linear fluid dynamics, various input constraints (e.g., backlash, deadzone, and saturation), and the complexities of unmodeled uncertainties and closed-chain mechanisms, particularly as the number of degrees of freedom (DoF) increases [1], [5]. Thus, building a high-performance controller with subcentimeter accuracy is critically important for the autonomous operation of heavy-duty hydraulic manipulators (HHMs).

Numerous studies have addressed the control challenges of hydraulically actuated manipulators in free-motion tasks. Various approaches have been employed for joint motion control, including adaptive control [5], adaptive robust control [6], neuroadaptive backstepping sliding mode control [7], model predictive control [8], and intelligent control methods, such as reinforcement learning [9] and radial basis function neural networks [10]. Another widely used approach is virtual decomposition control (VDC) [11] for the motion control of hydraulic manipulators [12], [13]. The focus on free-motion control is due to the prevalence of optimization-based, collision-free trajectory generation in path planning for autonomous operations within known or partially known environments [14], [15]. However, in unstructured environments, collision avoidance is challenging due to the lack of precise environmental knowledge. Even in fully known environments, tracking errors in the system can lead to unintended contact, which can cause irreparable damage to both the robot and the environment, especially in heavy-duty operation with huge interaction forces. Therefore, designing impact-resilient controllers or developing collision-inclusive motion planning to reduce the contact impact in contact-rich operations is crucial and has garnered significant research attention [16], [17]. This article aims to address these issues in the context of HHMs by designing an impact-resilient control scheme.

Despite the industrial significance of HHMs, limited studies have focused on designing controllers for contact-rich manipulation tasks. In [18], a hybrid force/motion controller was developed for a backhoe excavator using the sliding mode approach. To address the contact problem during the shoveling phase of hydraulic mining machines, Qin et al. [19] proposed an adaptive, robust impedance controller. A VDC-based hybrid motion/force controller was designed in [20] for a 2-DoF HHM. An adaptive impedance controller for contact force tracking in hydraulic excavators was proposed in [21]. A stability-guaranteed impedance controller was designed in [22] to ensure the performance of the VDC scheme in the event of unexpected contacts. The

benefits of a backdrivable servo valve for impedance control were thoroughly analyzed and experimentally verified in [23]. The problem of contact with uncertain environments was addressed in [24] through the design of an adaptive impedance controller. Although these studies have conducted experiments to validate their results, they typically focused on manipulators with fewer than 3 DoFs, simplifying the implementation. However, in real-world applications, enhancing the dexterity of manipulators often requires a higher number of DoFs, which increases system complexity and complicates the implementation of the designed controllers. Thus, there is a critical need for a high-precision, impact-resilient controller that can be feasibly implemented on high-DoF HHMs in industrial applications. In this study, by extending our previous research [25], which only considered free-motion tasks, a VDC-based, impact-resilient controller is designed to address these issues.

A key challenge in impact-resilient control design for HHMs is measuring contact force. Placing 6-DoF force/torque sensors on the end-effector of HHMs is not always feasible due to factors, such as high costs, potential damage to the sensors during operations, and the complexity of their retrofitting. One of the well-known approaches for external force/torque estimation is generalized momentum observer (GMO) [23], [26], which requires a Lagrangian representation of system dynamics. As the baseline controller in this study, the VDC scheme uses Newton–Euler (NE) approach to represent the dynamics of the system in Plücker coordinates. Therefore, direct integration of GMO and VDC could result in computational inefficiencies and complicate real-time implementation due to the necessity of dual model representations. Given the exceptional performance of the VDC in HHM applications [12], [13], [25] and its widespread use in diverse fields [27], [28], [29], addressing the aforementioned challenge becomes imperative. Existing solutions, such as the gravity-compensation-based estimator [20], circumvent some of these challenges by ignoring inertial and centrifugal effects, which is effective at low speeds. In addition, it requires Lagrangian-based gravity vector derivations, which is incompatible with the VDC context. Recognizing the systematic advantages of VDC in modeling, control, and stability analysis for complex systems, this article proposes a novel GMO-based force estimator introduced in Plücker coordinates to tackle the issues described above.

Considering the aforementioned issues, the current work designs a novel force-sensorless impact-resilient controller for generic 6-DoF real-world HHM with anthropomorphic arm and spherical wrist. The proposed high-level impact-resilient command is executed by joint-level, robust neuroadaptive controller, designed in our previous work [25]. Moreover, new formulation for GMO is introduced in the Plücker coordinate that refines the GMO and VDC integration, making it suitable for real-world implementation. Furthermore, the robustness and stability of the system under designed controller are proved by means of virtual stability and virtual power flow (VPF) concepts. Consequently, the contributions of the current work can be expressed as follows.

- 1) A force-sensorless impact-resilient method is proposed for full-pose control of a generic 6-DoF industrial HHM

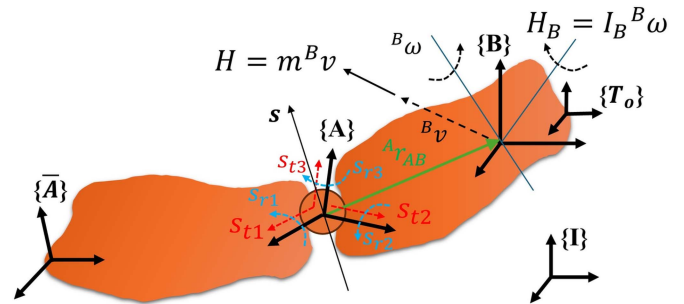


Fig. 1. Interconnected rigid bodies with attached Plücker coordinates.

with an anthropomorphic arm and spherical wrist, demonstrating the method's general applicability.

- 2) For the first time, a GMO-based force estimator is developed in Plücker coordinates and embedded into VDC.
- 3) Extensive real-time experiments and simulation comparisons are conducted on full-scale 6-DoF industrial HHM to show the performance and universality of the scheme.

The rest of this article is organized as follows. Section II expresses the fundamental mathematics of 6-D vectors. Section III describes the impact force estimation developed in Plücker coordinate. In Section IV, the details of the proposed impact-resilient controller and stability analysis are expressed. The experimental results are provided in Section V. Section VI presents additional performance evaluation. Finally, Section VII concludes this article.

II. MATHEMATICAL FORMULATION AND FOUNDATIONS

A. Spatial Force and Velocity Vectors in Plücker Coordinates

In contrast to Cartesian coordinates, Plücker coordinates are represented with a 6-D Plücker basis, resulting in a compact formulation of the system dynamics [30]. By employing the Plücker coordinates, the angular/linear motion and force/torque vectors can be represented in a single 6-D vector. In these coordinates, \mathcal{M}^6 represents the spatial motion vector space, and its dual space \mathcal{F}^6 represents the spatial force vector space. Consequently, for any given frame {A} (see Fig. 1), the spatial velocity vector ${}^A\mathcal{V} \in \mathcal{M}^6$ and spatial force vector ${}^A\mathcal{F} \in \mathcal{F}^6$ can be expressed as follows [11]:

$${}^A\mathcal{V} = [{}^A v, {}^A \omega]^T, \quad {}^A\mathcal{F} = [{}^A f, {}^A m]^T$$

with ${}^A v$ and ${}^A \omega$ being two 3-D coordinate vectors as linear and angular velocities, respectively, and ${}^A f$ and ${}^A m$ being 3-D coordinate vectors representing linear force and moment, respectively, of frame {A}, all of which are first expressed in inertial frame {I} and then transformed into frame {A} (see [11, Sect. 2.5.1]). It is assumed that each joint only allows a single degree of motion freedom, so that the spatial velocity vector can be described as

$${}^A\mathcal{V} = s \dot{q} + \bar{A}\mathcal{V} \quad (1)$$

with $\dot{q} \in \mathfrak{R}$ being joint velocity, ${}^A\mathcal{V}$ being spatial velocity of the previous bodies expressed in frame $\{A\}$, and $s = [s_t^T, s_r^T]^T$ being unit vector that determines the axis of the joint motion (as depicted in Fig. 1), with s_t being the translation vector and s_r being the rotation vector. The transformation matrix that transforms spatial force and velocity vectors between frames $\{A\}$ and $\{B\}$ (which coincides with the center of mass of the rigid body) is [11]

$${}^A U_B = \begin{bmatrix} {}^A R_B & \mathbf{0}_{3 \times 3} \\ ({}^A r_{AB} \times) {}^A R_B & {}^A R_B \end{bmatrix} \quad (2)$$

where ${}^A R_B \in \mathfrak{R}^{3 \times 3}$ is a rotation matrix between frame $\{A\}$ and $\{B\}$, and ${}^A r_{AB} = [r_x, r_y, r_z]^T$ denotes a vector from the origin of frame $\{A\}$ to the origin of frame $\{B\}$, expressed in $\{A\}$ with (\times) operator defined in Appendix A. Consequently, the spatial force and velocity vectors can be transformed between frames, as [11]

$${}^B \mathcal{V} = {}^A U_B^T {}^A \mathcal{V}, \quad {}^A F = {}^A U_B {}^B F. \quad (3)$$

B. Momentum

For the given rigid body configuration in Fig. 1 with attached frames of $\{A\}$ and $\{B\}$ and given spatial velocity ${}^B \mathcal{V} = [{}^B v, {}^B \omega]^T$ with inertial parameters m and I_B as mass and rotational inertia, respectively, the linear and angular momentum can be defined as $H = m {}^B v$ and $H_B = I_B {}^B \omega$, respectively. As the spatial momentum vectors $\bar{H}_B = [H^T, H_B^T]^T$ are the elements of \mathcal{F}^6 , they have the same algebraic properties as other spatial force vectors. Therefore, the spatial momentum vector of frame $\{A\}$ can be described as follows:

$$H_A = {}^A U_B \bar{H}_B = ({}^A U_B M_B {}^A U_B^T) {}^A \mathcal{V} = M_A {}^A \mathcal{V} \quad (4)$$

with $M_B = \text{diag}([m \cdot I_3, I_B])$, and M_A can be derived by performing matrix multiplication

$$M_A = \begin{bmatrix} m_A I_3 & -m_A ({}^A r_{AB} \times) \\ m_A ({}^A r_{AB} \times) & I_A \end{bmatrix} \quad (5)$$

with $I_A = {}^A R_B I_B {}^A R_B^T - m ({}^A r_{AB} \times)^2$. Equation (5) is the general expression for spatial inertia matrix in Plücker coordinates.

C. Rigid Body Dynamics

The dynamic equation of the rigid body in space, shown in Fig. 1, which is based on unique inertial parameter vector function $\phi(m, {}^A r_{AB}, I_A) \in \mathfrak{R}^{10}$ expressed in frame $\{A\}$, can be written as [31]

$$M_A \frac{d}{dt} ({}^A \mathcal{V}) + C_A ({}^A \omega) {}^A \mathcal{V} + G_A + \Delta_A = {}^A F^* \quad (6)$$

where $M_A \in \mathfrak{R}^{6 \times 6}$ is the mass matrix, $C_A \in \mathfrak{R}^{6 \times 6}$ is the centrifugal and Coriolis matrix, $G_A \in \mathfrak{R}^6$ is the gravity vector, $\Delta_A \in \mathcal{F}^6$ is uncertainty stemming from the rigid body model, and ${}^A F^* \in \mathcal{F}^6$ is the net spatial force vector applied to body.

Property 1: For a given rigid body dynamics (6), the following property holds:

$$\bar{Y}_A \phi_A = M_A \frac{d}{dt} ({}^A \mathcal{V}) + C_A ({}^A \omega) {}^A \mathcal{V} + G_A$$

with $\bar{Y}_A ({}^A \dot{\mathcal{V}}, {}^A \mathcal{V}) \in \mathfrak{R}^{6 \times 10}$ being regression matrix and $\phi_A(m, {}^A r_{AB}, I_A)$ being unique inertial parameter vector [31].

In the VDC approach, the required velocity plays an important role by encompassing the desired velocity along with one or two error terms related to the position or force error in the position or complaint control mode, respectively. Considering joint space required velocity as \dot{q}_r , which will be defined based on a given task, and computing the spatial velocities (${}^A \mathcal{V}_r$) of the connected rigid bodies and exploiting Property 1, the required net force/moment vector can be defined as [31]

$${}^A F_r^* = Y_A \hat{\phi}_A + {}^A F_c \quad (7)$$

where ${}^A F_c$ is the feedback control term and $Y_A \hat{\phi}_A$ is the feedforward term, where $\hat{\phi}_A$ is the estimation of ϕ_A and $Y_A ({}^A \dot{\mathcal{V}}_r, {}^A \mathcal{V}_r)$ is in the sense of Property [1] by replacing spatial velocity with required spatial velocities.

D. Radial Basis Functions Neural Networks

The approximation of the continues function Δ_A in (6), noted as $\hat{\Delta}_A$, can be done by the use of linearly parameterized neural networks and their universal approximation property

$$\hat{\Delta}_A = {}^A \hat{W}^T \Psi(\chi_A) + {}^A \varepsilon \quad (8)$$

with χ_A being the input vector, ${}^A \hat{W}$ being the updated weights, $\Psi(\chi_A)$ being the basis function in the form of Gaussian function, and ${}^A \varepsilon$ being approximation error with ${}^A \varepsilon \leq |{}^A \hat{\varepsilon}|$, where ${}^A \hat{\varepsilon}$ is an unknown, bound parameter. As it is shown in [25], by defining the adaptation laws as

$${}^A \dot{\hat{W}} = \Pi \left(\Psi(\chi_A) ({}^A \mathcal{V}_r - {}^A \mathcal{V})^T - \tau_0 {}^A \hat{W} \right) \quad (9)$$

$${}^A \dot{\hat{\varepsilon}} = \pi \left(({}^A \mathcal{V}_r - {}^A \mathcal{V}) - \pi_0 {}^A \hat{\varepsilon} \right) \quad (10)$$

with Π, π_0, τ_0 , and π being positive constants, the semiglobal uniformly ultimate boundedness (SGUUB) of the system can be ensured under unknown model uncertainties.

E. Natural Adaptation Law (NAL)

For the given rigid body in space, shown in Fig. 1, with an inertial frame $\{A\}$, there is a unique inertial parameters $\phi_A \in \mathfrak{R}^{10}$ that satisfy physical consistency conditions. As it is detailed in [31] and [32], there is a one-to-one linear map $f : \mathfrak{R}^{10} \rightarrow S(4)$, such that

$$f(\phi_A) = \mathcal{L}_A = \begin{bmatrix} 0.5 \text{tr}(I_A) \cdot \mathbf{1} - I_A & h_A \\ h_A^T & m_A \end{bmatrix}$$

$$f^{-1}(\mathcal{L}_A) = \phi_A(m_A, h_A, \text{tr}(\Sigma_A) \cdot \mathbf{1} - \Sigma_A)$$

where m_A, h_A , and I_A are the mass, first mass moment, and rotational inertia matrix, respectively. $\mathcal{L}_A \in S(4)$ is a pseudoinertia matrix with $S(4)$ being the space of 4×4 real-symmetric matrices and $\Sigma_A = 0.5 \text{tr}(I_A) - I_A$.

For a given \mathcal{L}_A with its estimation $\hat{\mathcal{L}}_A$, the Lyapunov function can be defined in the form of Bregman divergence with the log-det function as

$$\mathcal{D}_F(\mathcal{L}_A \parallel \hat{\mathcal{L}}_A) = \log \frac{|\hat{\mathcal{L}}_A|}{|\mathcal{L}_A|} + \text{tr}(\hat{\mathcal{L}}_A^{-1} \mathcal{L}_A) - 4 \quad (11)$$

with

$$\dot{\mathcal{D}}_F(\mathcal{L}_A \parallel \hat{\mathcal{L}}_A) = \text{tr}([\hat{\mathcal{L}}_A^{-1} \dot{\hat{\mathcal{L}}}_A \hat{\mathcal{L}}_A^{-1}] \tilde{\mathcal{L}}_A)$$

being the time-derivative of (11), where $\tilde{\mathcal{L}}_A = \hat{\mathcal{L}}_A - \mathcal{L}_A$. Thus, the NAL can be derived as

$$\dot{\hat{\mathcal{L}}}_A = \frac{1}{\gamma} \hat{\mathcal{L}}_A \left(\mathcal{S}_A - \gamma_0 \hat{\mathcal{L}}_A \right) \hat{\mathcal{L}}_A \quad (12)$$

with $\gamma > 0$ being the adaptation gain for all the rigid bodies of the system and $\gamma_0 > 0$ being a small positive gain. In addition, \mathcal{S}_A is a unique symmetric matrix defined in [33].

F. Virtual Stability

The VDC approach divides a complex system into subsystems using virtual cutting points (VCPs), as illustrated in Fig. 2. A VCP forms a virtual cutting surface [see Fig. 2(b)] where spatial force vectors can be exerted from one part, which is interpreted as a driving VCP, to another, which is interpreted as a driven VCP, shown with green and red lines in Fig. 2(c), respectively. Once the system is decomposed by placing VCPs, control actions can be designed to meet subsystem-level objectives. Another key concept in VDC is VPF, which characterizes dynamic interactions among subsystems. Presented in Definition 1, the VPF represents the power transmission between the decomposed bodies, allowing to expand the virtual stability of subsystem to the stability of overall systems. In the followings, important definitions in the VDC context are provided.

Definition 1: With respect to frame $\{A\}$, the VPF is defined as the inner product of the spatial velocity vector error and the spatial force vector error [34], that is

$$p_A = ({}^A\mathcal{V}_r - {}^A\mathcal{V})^T ({}^A F_r - {}^A F)$$

where ${}^A\mathcal{V}_r \in \mathcal{M}^6$ and ${}^A F_r \in \mathcal{F}^6$ represent the required vectors of ${}^A\mathcal{V} \in \mathcal{M}^6$ and ${}^A F \in \mathcal{F}^6$, respectively.

Definition 2: A nonnegative accompanying function $\nu(t) \in \mathfrak{R}$ is a piecewise, differentiable function defined $\forall t \in \mathfrak{R}^+$ with $\nu(0) < \infty$ and $\dot{\nu}(t)$ exists almost everywhere.

Lemma 1 (See [25]): Consider a complex robot that is virtually decomposed into subsystems. Each subsystem is said to be virtually semiglobally uniformly ultimately bounded with its nonnegative accompanying function $\nu(t)$ and its affiliated vector $\dot{\nu}(t)$, if and only if

$$\dot{\nu} \leq -\alpha_1 \nu + \alpha_{10} + p_A - p_C \quad (13)$$

with α_1 and α_{10} being positive constants and p_A and p_C denoting the sum of VPFs in the sense of Definition 1 at frames $\{A\}$ (placed at driving VCPs) and $\{C\}$ (placed at driven VCPs), as shown in Fig. 2(c).

Theorem 1: Consider a complex robot [see Fig. 2(a)] that is virtually decomposed into subsystems [see Fig. 2(c)]. If all the decomposed subsystems are virtually semiglobally uniformly

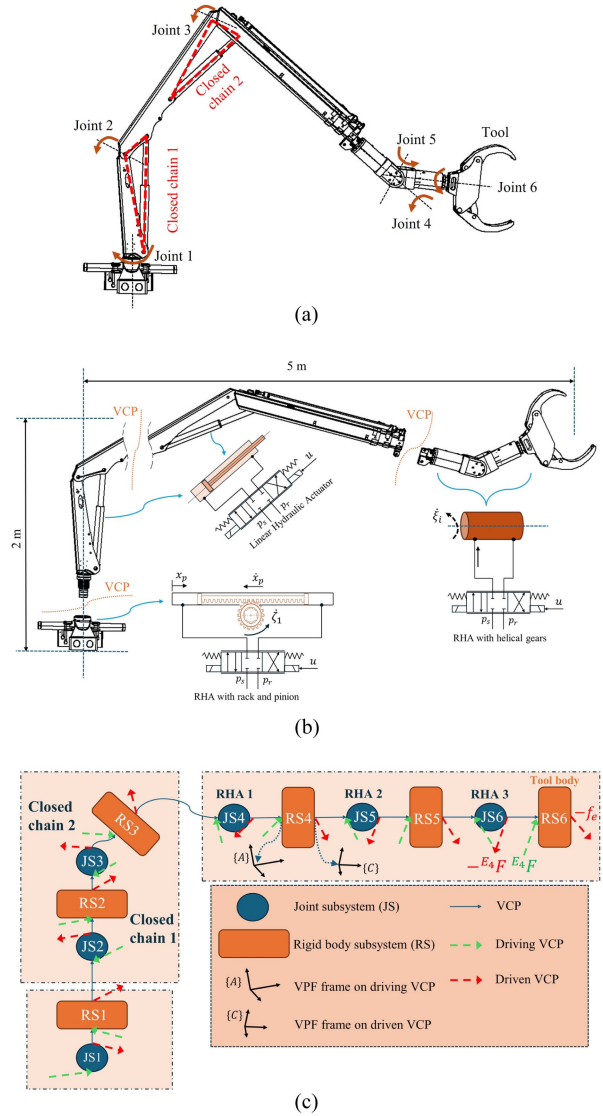


Fig. 2. Scheme of 6-DoF HMM with VDC approach. (a) General configuration of HMM. (b) Decomposition of HMM into subsystems. (c) Scheme of VDC with VCP concept.

ultimately bounded in the sense of Lemma 1, then the entire system has SGUUB [11], [25].

III. IMPACT FORCE ESTIMATION

At the time of impact, the environment shows impedance behavior, outputting force for the given input velocity. Such a behavior can be modeled as

$$M_f \ddot{X}_{ef} + D_f \dot{X}_{ef} + K_f \tilde{X}_{ef} = f_e \quad (14)$$

with M_f , D_f , and K_f being inertia, damping, and stiffness of environment, respectively, \tilde{X}_{ef} , \dot{X}_{ef} , and \ddot{X}_{ef} denoting the deformation, velocity, and acceleration of the environment, respectively. From (14), it can be concluded that by having the position and parameters of the environment, the contact force can be computed. However, in most of the real-world implementations, neither of the information is available, requiring

direct force estimation. In this section, a novel GMO-based force estimator is presented in Plücker coordinate to estimate the impact force at the time of contact based on joint measurements without requiring environmental information.

The current form of GMO for contact force estimation requires the Lagrangian representation of the robot dynamics as

$$M \ddot{x} + C(x, \dot{x}) \dot{x} + G(x) = \tau + J^T f_e \quad (15)$$

with M , C , and G being mass, centrifugal, and gravity matrices, respectively, τ is the input torque, f_e being the contact force, and J being the Jacobian matrix. Consequently, to design a contact force observer for VDC approach, it is required to derive two different dynamics model: the Lagrangian model (15) for observer design with complexity order (CO) of $O(n^2)$, and the NE model (6) for controller design with CO of $O(2n)$. In addition to the mathematical burden of deriving two dynamics, the computational cost of such an approach might engender problems in real-time implementation, especially for high-DoF HHMs. In this article, for the first time, we developed GMO in Plücker coordinate that matches the motion equations of VDC, reducing the total CO to $O(2n)$.

Consider a rigid body in space (see Fig. 1) represented in Plücker coordinate with spatial velocity and force vectors belonging to \mathcal{M}^6 and \mathcal{F}^6 , respectively. The momentum in the frame $\{A\}$ can be represented as (4) with time derivative

$$\frac{d}{dt} H_A = \frac{d}{dt} (M_A) {}^A \mathcal{V} + M_A \frac{d}{dt} ({}^A \mathcal{V}). \quad (16)$$

As the manipulator system is an interconnected multi rigid body, the contact at the end-effector will impact all the rigid bodies of the system. This impact can be detected by difference between the control action and the exact model of that body. We denote this impact as ${}^A F_d$

$${}^A F_d = M_A \frac{d}{dt} ({}^A \mathcal{V}) + C_A ({}^A \omega) {}^A \mathcal{V} + G_A + {}^A U_{T_o} {}^{T_o} F - {}^A F_r \quad (17)$$

with ${}^{T_o} F$ being the spatial force of successor body with respect to frame $\{T_o\}$ (see Fig. 1). In order to eliminate the need for time derivative of spatial inertial matrix in (16), we have

$$\frac{d}{dt} (M_A) = -({}^A \mathcal{V} \times)^T M_A - M_A {}^A \mathcal{V} \times \quad (18)$$

where the proof is provided in Appendix A. By replacing (17) and (18) in (16) with ${}^A \mathcal{V} \times {}^A \mathcal{V} = 0$, one can obtain

$$\begin{aligned} \frac{d}{dt} H_A = & -({}^A \mathcal{V} \times)^T M_A {}^A \mathcal{V} + {}^A F_r + {}^A F_d \\ & - C_A ({}^A \omega) {}^A \mathcal{V} - G_A - {}^A U_{T_o} {}^{T_o} F. \end{aligned} \quad (19)$$

The representation of momentum variation in each rigid body, as shown in (19), allows us to detect the impact of contact at each subsystem that matches the characteristics of the VDC context. By defining

$$\begin{aligned} {}^A \mathfrak{F} = & {}^A F_r - ({}^A \mathcal{V} \times)^T M_A {}^A \mathcal{V} \\ & - C_A ({}^A \omega) {}^A \mathcal{V} - G_A - {}^A U_{T_o} {}^{T_o} F \end{aligned} \quad (20)$$

one can rewrite (19) as

$${}^A F_d = \frac{d}{dt} H_A - {}^A \mathfrak{F}. \quad (21)$$

Now, the spatial residual vector \mathcal{R}_A can be defined as

$$\mathcal{R}_A = \mathbf{K} \left\{ H_A(t) - H_A(t_0) - \int_{t_0}^t ({}^A \mathfrak{F} + \mathcal{R}_A) dt \right\} \quad (22)$$

where $\mathcal{R}_A(t_0) = \mathbf{0}$ and \mathbf{K} is diagonal positive definite matrix. By taking the derivative of (22) and using (21), one can obtain

$$\frac{d}{dt} \mathcal{R}_A = -\mathbf{K} \mathcal{R}_A + \mathbf{K} {}^A F_d. \quad (23)$$

Finally, by taking the Laplace transform of (23), we have

$$\mathbf{r}_i(s) = \frac{\mathbf{K}_{ii}}{s_i + \mathbf{K}_{ii}} \hat{f}_i(s) \quad (24)$$

with $\mathcal{R}_A = [\mathbf{r}_1, \dots, \mathbf{r}_6]^T$ and ${}^A F_d = [\hat{f}_1, \dots, \hat{f}_6]^T$. Equation (24) demonstrates that by setting a high gain to \mathbf{K} , one can establish $\mathbf{r}_i \simeq \hat{f}_i$, indicating $\mathcal{R}_A \simeq {}^A F_d$.

The spatial residual \mathcal{R}_A captures the projection of the impact on a rigid body expressed in attached Plücker coordinate $\{A\}$. Thus, the accumulation of the projections over all the rigid bodies should be computed, from which the estimation of impact force can be reconstructed. For this aim, the map from Plücker coordinate to joint space, and from joint space to end-effector (where impact occurs) is required. The former one can be accomplished, after computing all spatial residuals for $A \in \mathfrak{G}$, by use of unit screw vector \mathbf{s} in (1) as

$$\mathbf{r}_A = \mathbf{s}^T \mathcal{R}_A \quad (25)$$

where \mathfrak{G} includes n Plücker frames attached to n joint of interconnected multibody system. Then, the latter one can be established as

$$\hat{f}_e = (J^T)^\dagger \mathbf{r} \quad (26)$$

with $\mathbf{r} = [r_1, \dots, r_n]^T$ computed through (25) for each r_i , and $(\cdot)^\dagger$ being the pseudoinverse (if nonsquare) of the Jacobian matrix $J \in \mathfrak{R}^{6 \times n}$. To avoid false alarm, the contact detection can be done whenever $\|\mathbf{r}\| > \bar{r}$, which $\bar{r} > 0$ is the threshold.

Remark 1: Spatial residual (22) only requires spatial vectors and matrices through (4) and (20) defined in the Plücker coordinate.

Remark 2: The derivative of the spatial inertial matrix in (18) is a general expression for any given frame $\{A\}$. This term will vanish for local frames that are attached to the body and moves with body motion.

IV. IMPACT RESILIENT CONTROL DESIGN AND STABILITY ANALYSIS

In our latest work [25], we conducted a comprehensive analysis of kinematics and dynamics for HHM represented in Fig. 2, and designed a control action for free-motion tasks. Building upon this foundation, our current work extends those findings to develop an impact-resilient control scheme. Specifically, we redefine the required velocity \dot{q}_r to meet free-motion and contact-rich tasks objectives, following a similar approach

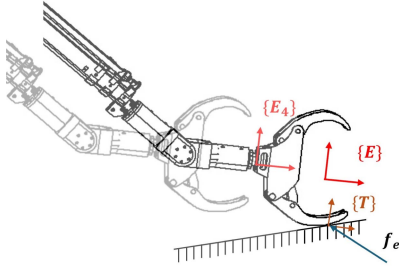


Fig. 3. End-effector of HHM approaching an environment.

to [22]. The new required velocity definition will be integrated into the existing neuroadaptive, orchestrated robust controller from [25].

A. Impact Resilient Control

The pose and velocity of the end-effector can be written as a function of joint angles q

$$\mathcal{X} = \mathcal{N}(q), \quad \dot{\mathcal{X}} = J(q)\dot{q} \quad (27)$$

where $\mathcal{N}(\cdot)$ shows forward kinematics of the manipulator and \dot{q} being joint velocity vector. In addition, the desired impedance behavior can be rewritten as

$$D_d(\dot{\mathcal{X}}_d - \dot{\mathcal{X}}) + K_d(\mathcal{X}_d - \mathcal{X}) = -(f_{ed} - f_e) \quad (28)$$

where D_d and K_d being the desired damping and stiffness matrices, respectively, $\mathcal{X}_d \in \mathbb{R}^6$ and $\dot{\mathcal{X}}_d \in \mathbb{R}^6$ being the desired pose and desired velocity of end-effector, respectively, and $f_e \in \mathbb{R}^6$ being the contact force (see Fig. 3). As it was mentioned, required velocity plays an important role in VDC context, which can be defined based on free-motion or in-contact tasks. In this work, in order to achieve the desired impedance (28), the required Cartesian space velocity is defined as

$$\dot{\mathcal{X}}_r = \dot{\mathcal{X}}_d + \Gamma(\mathcal{X}_d - \mathcal{X}) + \Sigma(f_{ed} - \hat{f}_e) \quad (29)$$

with f_{ed} being the desired contact force and \hat{f}_e being the estimated contact force (26). In addition, $\Gamma \in \mathbb{R}^{6 \times 6}$ and $\Sigma \in \mathbb{R}^{6 \times 6}$ are positive-definite matrices. The task space tracking error is $e = \mathcal{X}_d - \mathcal{X} = [e_p^T, e_o^T]^T$, with $e_p \in \mathbb{R}^3$ being the position error, whereas $e_o \in \mathbb{R}^3$ being the orientation error defined based on quaternions as

$$e_o = \eta(q)\epsilon_d - \eta_d\epsilon(q) - \mathbf{S}(\epsilon_d)\epsilon(q) \quad (30)$$

where $\eta(q)$ and $\epsilon(q)$ are the unit quaternions computed from the rotation matrix, and η_d and ϵ_d are the desired unit quaternions. As stated in [22], to establish the desired impedance by means of (29), the following condition must be ensured:

$$\Gamma = K_d D_d^{-1} \quad (31)$$

$$\Sigma = D_d^{-1}. \quad (32)$$

Now, by using the Jacobian matrix, the required joint velocity can be achieved

$$\dot{q}_r = (J)^\dagger \dot{\mathcal{X}}_r. \quad (33)$$

The required joint velocity in (33) conveys the desired impedance to subsystem level, where the control law is designed to establish it, as shown in Fig. 4.

Considering the concept of VPF in VDC, contact only affects the stability of the tool object, which requires attention. Consequently, in the following section, the control design and stability of the tool body will be examined, while the control and stability of the rest of the system is the same as [25] (Fig. 4 displays the control scheme). This highlights the unique feature of the VDC approach, wherein alterations in one subsystem do not affect the stability of other subsystems.

B. Rigid Body Control Design

Considering Fig. 3, frame $\{T\}$ represents contact point at the end-effector, frame $\{E\}$ represents the tip of end-effector, and frame $\{E_4\}$ is the body frame of the tool. Then, the spatial velocity vector of frame $\{T\}$ can be written as

$${}^T\mathcal{V} = N_c \dot{\mathcal{X}} \quad (34)$$

with N_c mapping the end-effector velocity to the spatial velocity of the tool tip. Then, the spatial velocity of the tool can be derived as

$${}^{E_4}\mathcal{V} = {}^T U_{E_4}^T {}^T\mathcal{V}. \quad (35)$$

Accordingly, the spatial force vector of the tool can be written as

$${}^T F = N_c f_e. \quad (36)$$

The net spatial force vector ${}^{E_4}F^*$ of the tool can be written as

$$M_{E_4} \frac{d}{dt} ({}^{E_4}\mathcal{V}) + C_{E_4} ({}^{E_4}\omega) {}^{E_4}\mathcal{V} + G_{E_4} + {}^{E_4}\Delta_R(t) = {}^{E_4}F^*. \quad (37)$$

In addition, the force resultant on the tool body can be written

$${}^{E_4}F_r^* = {}^{E_4}F - {}^{E_4}U_T {}^T F. \quad (38)$$

By following the same procedure in (34)–(36) for required terms, one can obtain:

$${}^T\mathcal{V}_r = N_c \dot{\mathcal{X}}_r \quad (39)$$

$${}^{E_4}\mathcal{V}_r = {}^T U_{E_4}^T {}^T\mathcal{V}_r \quad (40)$$

$${}^T F_r = N_c f_{ed} \quad (41)$$

with $\dot{\mathcal{X}}_r$ defined in (29). Finally, the required net force vector can be expressed in the sense of (7) as

$${}^{E_4}F_r^* = Y_{E_4} \hat{\phi}_{E_4} + K_{E_4} ({}^{E_4}\mathcal{V}_r - {}^{E_4}\mathcal{V}) + \hat{\Delta}_R \quad (42)$$

with $\hat{\Delta}_R$ being the estimated model uncertainty, in the sense of Section II-D. As a result, the required spatial force vector, which acts as the control signal for rigid body, can be written as

$${}^{E_4}F_r = {}^{E_4}F_r^* + {}^{E_4}U_T {}^T F_r. \quad (43)$$

The required spatial force vector in (43) represents the term accounting for both free-motion and in-contact operations. This force must be generated by the corresponding actuator subsystem, as illustrated in Fig. 2(b) and detailed in [25].

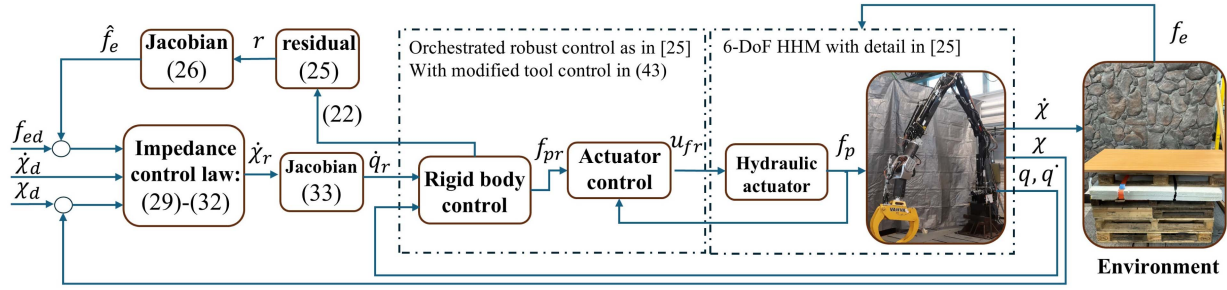


Fig. 4. Impact resilient control scheme. The impedance law \dot{x}_r , computed in (29), is transformed into joint space command \dot{q}_r , which is executed by the control approach in [25]. The actuator-level control command, u_{fr} , being desired voltage, is designed to generate required piston force f_{pr} , accomplishing control objectives. The command u_{fr} controls the hydraulic valves. Please see [25] for detailed explanation.

C. System Stability

Due to environmental contact, the second term in (38) is nonzero, differing from the free-motion condition in [25]. Consequently, only the virtual stability of the tool needs to be ensured under these contact conditions, while the stability of the rest of the system is the same as in [25].

Theorem 2: Consider the tool body with governing dynamics of (37), control action of (42) and (43), and adaptation law of (12) (by replacing $\{A\}$ with $\{E_4\}$). By defining the accompanying function in the sense of Lemma 1 as

$$\begin{aligned} \nu_1 = & \frac{1}{2} (E_4 \mathcal{V}_r - E_4 \mathcal{V})^T M_{E_4} (E_4 \mathcal{V}_r - E_4 \mathcal{V}) \\ & + \gamma \mathcal{D}_F(\mathcal{L}_{E_4} \|\hat{\mathcal{L}}_{E_4}) + \frac{1}{2} \text{tr}(E_4 \tilde{W}^T E_4 \Gamma^{-1} E_4 \tilde{W}) \\ & + \frac{1}{2 E_4 \pi} E_4 \tilde{\varepsilon}^T E_4 \tilde{\varepsilon} \end{aligned} \quad (44)$$

where $\tilde{(\cdot)} = (\cdot) - \hat{(\cdot)}$, and its time derivative

$$\dot{\nu}_1 \leq -\alpha \nu_1 + \alpha_0 + p_{E_4} - p_T \quad (45)$$

the virtual SGUUB of the tool body subsystem can be ensured.

Proof 1: Taking the time derivative of (44) and using (9), (10), (12), (37), (42), (43), and following the same procedure in [25, Appendix A], one can obtain (45).

As it can be seen from (45) and Fig. 2(c), the p_{E_4} is the VPF from the preceding subsystem and will be canceled out, as shown in [25]. In contrast, p_T is VPF resulting from end-effector interaction with environment, which is critical and must be addressed.

Lemma 2: Defining the impedance control command in the sense of (29) with (31) and (32) results in

$$p_T = 0.$$

Proof 2: See Appendix B.

Theorem 3: Consider the HHM in Fig. 2(a), which is decomposed into subsystem in Fig. 2(c). The entire system is SGUUB under impedance control law (29) with all the adaptation laws.

Proof 3: See Appendix C.

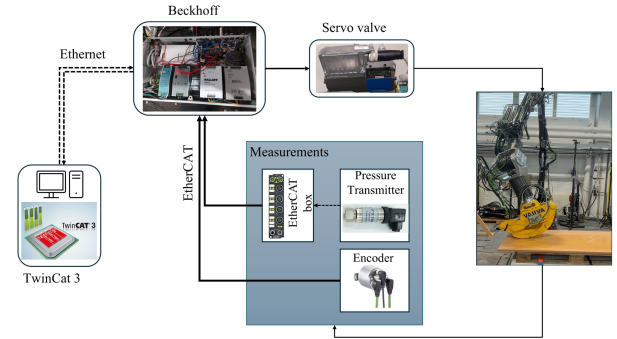


Fig. 5. Experimental setup.

V. EXPERIMENTAL RESULTS

This section presents the results of real-time implementation of the designed impact-resilient controller, with the detail of control scheme represented in Fig. 4.

A. Experimental Setup

Fig. 5 demonstrates the setup for real-time implementation. Druck PTX1400 and Unik 5000 pressure transmitters (range 25 MPa) and Sick afS60 (18-bit) absolute encoders are utilized in the experiments. In addition, EP3174-0002 EtherCAT module has been utilized to convert the analog pressure data to digital data, which can be read by Beckhoff platform. The Bosch Rexroth NG6 size servo solenoid valve with 12 l/min for base actuator, 100 l/min for second and third actuators, and 40 l/min for the Eckart wrist, all at $\Delta P = 3.5$ MPa per notch, are utilized to control the flow. A couple of wooden pallets are utilized to represent the unknown environment (see Fig. 5) for in-contact experiments. The entire controller is designed in the host PC with Intel Core i7-6700 CPU 3.40 GHz, and uploaded to the Beckhoff platform with Intel Core i7 2610UE 1.5 GHz for real-time implementation with 1ms sample time. Human-machine interface has been designed in TwinCAT 3.

B. Scenarios of Experiments

In order to vastly examine the outcomes of this article, two sets of experiments are conducted: free-motion and in-contact

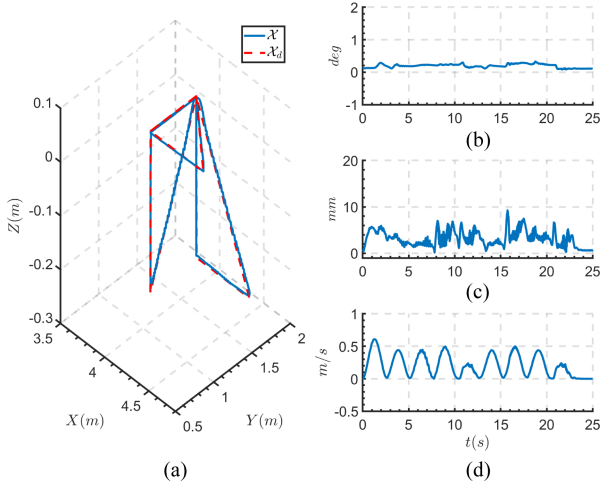


Fig. 6. Path tracking with $t_f = 2.5$ s. (a) Desired pose tracking. (b) RMS of orientation error. (c) RMS of position error. (d) Norm of end-effector velocity.

experiments. In all the experiments, the manipulator starts from the rest point and follows the desired trajectory. A smooth fifth-order trajectory generator is utilized to produce a smooth trajectory between the set points for a given execution time, t_f . The smaller the t_f , the faster the trajectory. In all the experiments, different trajectories with different speeds are designed to better evaluate the performance and robustness of the controller. In all the contact experiments, the manipulator makes a contact in the y -direction with the wooden pullets (see Fig. 5) while tracking the desired trajectory with wrist-down configuration. This scenario reflects the pick and place task, which is a relevant application in real-world cases.

C. Free-Motion Performance

The control gains have been selected as follows to get the best tracking result: $K_d = [1, 0.9, 0.7, 1.2, 1.2, 1.2] \cdot 10^6$, $D_d = [1, 1, 1, 1, 1, 1] \cdot 10^5$, $K_{E4} = 50 \cdot I$, $\gamma = 500$, $\Pi = 300$, $\pi = 10$, and low-level control gains as in [25]. Fig. 6(a) demonstrates the path tracking performance with the desired values in Cartesian space for $t_f = 2.5$ s. Fig. 6(b) shows the root mean square (rms) of orientation error, Fig. 6(c) depicts the rms of position error, and Fig. 6(d) displays the norm of end-effector velocity. As can be seen, the total rms of less than a 0.5° for orientation and less than 1 cm for position indicates that the subcentimeter tracking accuracy has been preserved for position.

One of the well-known indexes to evaluate the performance of the controller in free-motion tasks is ρ value [1]

$$\rho = \frac{|e|_{\max}}{|\dot{\mathcal{X}}|_{\max}}. \quad (46)$$

The ρ value indicates the importance of low tracking error in higher velocities, which is utilized to compare the result of this study with previous studies. Fig. 7(a) illustrates the result of fast trajectory tracking ($t_f = 1.5$ s) of triangular path in the x - y plane while orientation and the z -direction position are active and in the set-point control mode. Fig. 7(b) depicts the rms error of

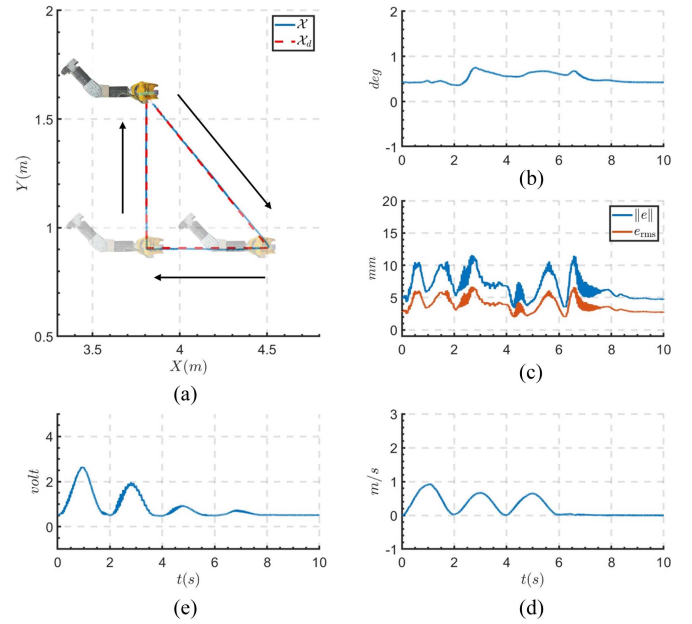


Fig. 7. Path tracking with $t_f = 1.5$ s. (a) Desired pose tracking. (b) RMS of orientation error. (c) Norm and rms of position error with blue and red line, respectively. (d) Norm of end-effector velocity. (e) Norm of voltage command.

TABLE I
PERFORMANCE INDEX EVALUATION OF CARTESIAN SPACE

Study	ρ	DoF*	ρ/DoF
This study	0.0124	6	0.0021
Koivumaki 2015 [12]	0.005	2 $^\diamond$	0.0025
Koivumaki 2019 [13]	0.0057	2 $^\diamond$	0.0029
Kalmari 2015	0.12 $^\top$	3 ‡	0.04
Zhu 2005	0.015 $^\top$	3 ‡	0.005
Tsukamoto 2002	0.126 $^\top$	6	0.021

* DoF in Cartesian space with 3 DoF for position and 3 DoF for orientation.

$^\diamond$ Only x - and y - directions were considered.

$^\top$ Reported in [1].

‡ Only position of end-effector was considered.

The bold values are the results of the present work and are used only to separate and highlight the superiority of our results compared to other works.

orientation regulation (which is still less than a degree), Fig. 7(c) shows the rms (red line) and norm (blue line) of the position error, the norm of the end-effector velocity is exhibited in Fig. 7(d), and the norm of the voltage commands to all the values is demonstrated in Fig. 7(e). The maximum norm of the position error is 11.5 mm at the maximum velocity of the 0.93 m/s, resulting in $\rho = 0.0124$ s. Note that the maximum value of rms error is almost 5 mm, representing excellent performance of the proposed method.

Table I provides the comparison of the results with previous studies based on the number of active Cartesian space DoFs. As can be seen, the achieved result of the present article outperforms other approaches. Establishing such a result for a real-world HHM (with weight of 650 kg at 4 m reach) demonstrates the excellent performance of the proposed method and its universality and reliability in real-world applications. Such an excellent

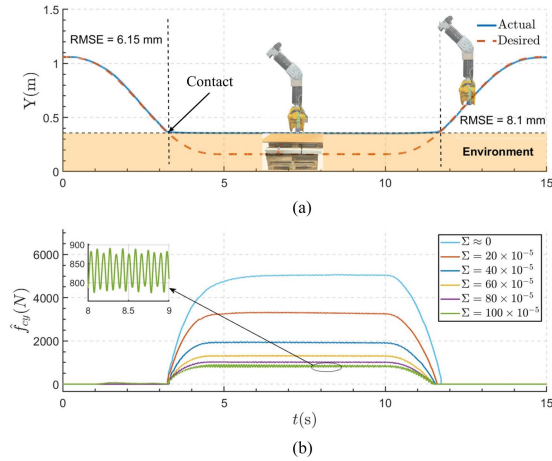


Fig. 8. Estimated impact force with various Σ . (a) Path tracking in direction with contact. (b) Estimated forces.

performance of the controller allows for fast detection of impact force at the time of contact, enabling the controller to respond quickly to mitigate potential damage to both the manipulator and the environment. This rapid detection and response mechanism contributes significantly to the system’s resilience, especially during impact scenarios.

D. In-Contact Performance

In this section, the performance of the controller in contact-rich operations is experimentally investigated. The control gains are the same as previous section with $K_d = \text{diag}([1, 0.0075, 0.7, 1.2, 1.2, 1.2]) \cdot 10^6$. To evaluate the impact-resiliency of the controller—defined as its ability to mitigate the adverse effects of unintended contact while maintaining high pose-tracking accuracy—we conducted the experiment, as illustrated in Fig. 8. In this experiment, the HHM follows a desired trajectory and makes contact with an unknown environment. The case with $\Sigma \approx 0$ represents the free-motion controller, whereas other values of Σ equip the controller with impact-resiliency. As depicted in Fig. 8(b), the impact-resilient approach achieves a significant reduction in contact force by 80% (from 5 to 1 kN) without compromising position-tracking accuracy, as shown in Fig. 8(a). This substantial reduction in impact force, combined with subcentimeter position-tracking precision, underscores the effectiveness of the proposed controller in minimizing damage during contact events while maintaining tracking performance. For the rest of the experiments, we use $\Sigma = [1, 60, 1, 1, 1, 1]^T \cdot 10^{-5}$ corresponding to $D_d = \text{diag}([1, 0.0167, 1, 1, 1, 1]) \cdot 10^5$.

Fig. 9(a) illustrates the pose tracking of the end-effector with an unexpected contact with unknown environment. As can be seen, the tracking error in Fig. 9(c) in noncontact directions (x and z) are less than a centimeter for $t_f = 5$ s and orientation error in Fig. 9(d) is less than a 0.5° . Fig. 9(b) also shows the estimated contact force in the contact direction (\hat{f}_{cy}). In order to display the robustness and stability of the controller, the same experiment

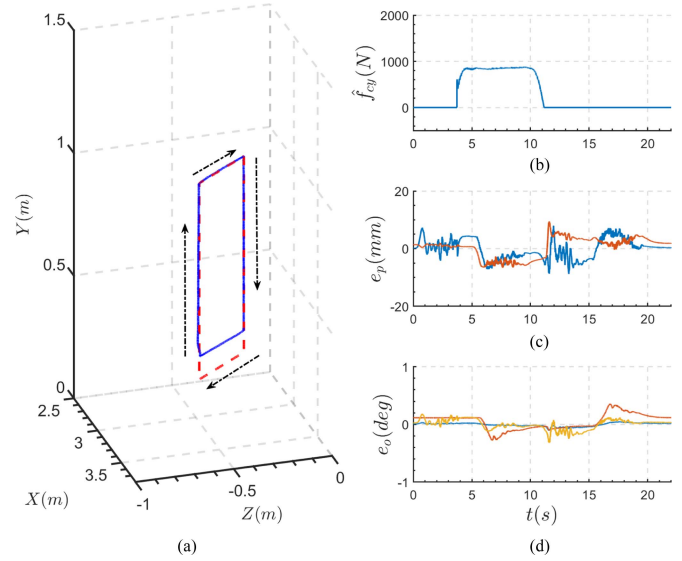


Fig. 9. (a) Path tracking in Cartesian space with contact. (b) Impact force. (c) Position error in noncontact directions. (d) Orientation error.

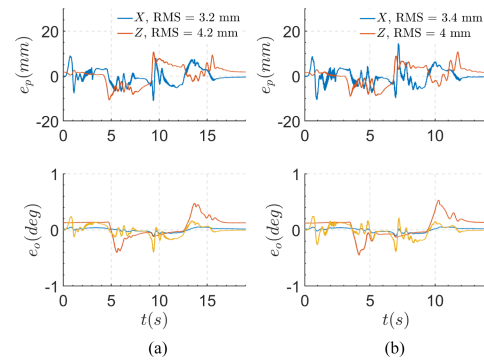


Fig. 10. Position and orientation tracking during contact. (a) Position and orientation errors for $t_f = 4$ s. (b) Position and orientation errors for $t_f = 3$ s.

with $t_f = 4$ s and $t_f = 3$ s, which are faster trajectories, is performed. As can be seen from Fig. 10, the orientation and position error in noncontact directions are less than a 0.5° and 1 cm, respectively, despite of following a fast trajectory in presence of contact. All the results, demonstrates the impact-resiliency of the system (robustness to the different contact speeds and unknown environment) with high-performance tracking, thanks to baseline neuroadaptive controller in [25].

In many industrial contact-rich scenarios, dexterous operations may be required while maintaining contact with the environment. Successfully performing such tasks necessitates establishing safe contact and achieving precise control accuracy. Figs. 11 and 12 examine the wrist maneuvering of the HHM during contact. As before, the manipulator follows the desired trajectory and makes a contact, after which the wrist maneuvering starts. As shown, excellent orientation accuracy is achieved across different maneuvering scenarios with no pulse contact forces.

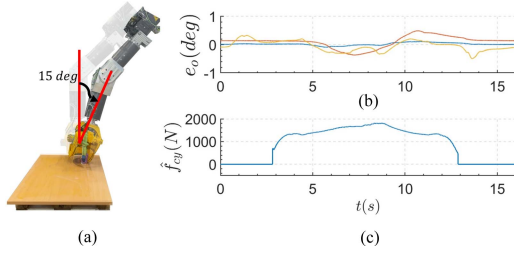


Fig. 11. (a) Wrist maneuvering during the contact with $t_f = 4$ s. (b) Orientation error. (c) Contact force.

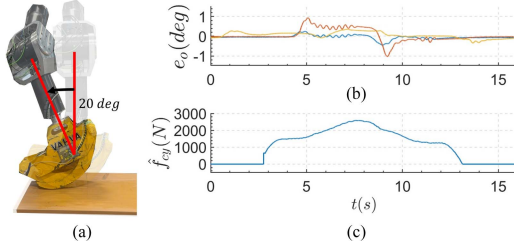


Fig. 12. (a) Wrist maneuvering during the contact with $t_f = 4$ s. (b) Orientation error. (c) Contact force.

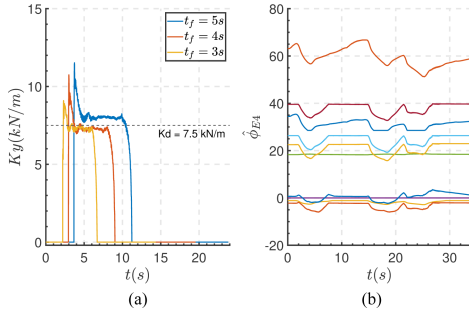


Fig. 13. (a) Rendered stiffness in contact direction. (b) Time history of $\hat{\phi}_{E4}$.

In addition, Fig. 13(a) presents the time history of the stiffness rendered by the manipulator during contact at different velocities. It can be observed that the manipulator's behavior during contact closely matches the desired stiffness ($K_y \cong K_{dy}$) with accuracies of 6%, 2%, and 2% for $t_f = 5$, 4, and 3 s, respectively. Moreover, the adaptation signals for the unknown rigid body parameters are shown in Fig. 13(b), demonstrating the boundedness of the estimated parameters.

VI. SIMULATION COMPARISON

For further performance evaluation, simulation results are provided in this section. To evaluate the accuracy of the proposed force estimator, the Simscape toolbox of SIMULINK along with the manipulator's 3-D model parameters is utilized to simulate the system in the contact with an environment. The simulation scenario was the same, as shown in Fig. 8. The achieved rms of error between the estimated force from proposed algorithm and the ground truth force from Simscape is 41.8 N with the

TABLE II
IMPACT-RESILIENCY COMPARISON OF DIFFERENT CONTROLLERS

Controller	E_0 (deg)	E_{pxz} (mm)	E_{py} (mm)	f_{ep}	u
This study	0.25	6.11	33.03	246.3	0.276
[23]	2.38	42.9	87.32	843.2	0.248
[18]	1.78	38.43	52.39	453.6	0.245
[22]	1.56	26.77	46.53	558.31	0.245
PID	0.83	91.9	112.16	739.5	0.265

The bold values are the results of the present work and are used only to separate and highlight the superiority of our results compared to other works.

steady-state error of 18 N, showing the acceptable accuracy of the force estimator.

In addition, Table II depicts the comparison of the proposed method with existing impedance controllers. The comparison is conducted based on position tracking accuracy, peak pulse force, and control effort. All simulations are conducted in SIMULINK, incorporating 10% parametric uncertainty and compound input nonlinearities, with a sample time of 1 ms to emulate the real-world condition. In the table, E_0 , E_{pxz} , and E_{py} represent rms of orientation, position in noncontact direction, and position in contact direction errors, respectively, where f_{ep} and u represent peak pulse force at the time of contact and rms of total control voltage, respectively. As can be seen from the table, the proposed method established high-accuracy position tracking while having a less peak force for given almost the same voltage signal.

Finally, to demonstrate the reduced computational cost achieved by the proposed method, we conducted simulations on a personal laptop equipped with an Intel Core i7-13700H CPU (2.4 GHz). The simulations were performed under the same conditions, as shown in Fig. 9, but using two different observer algorithms: the proposed observer in Plücker coordinates and the commonly used GMO in the Lagrangian formulation. The runtime-to-simulation ratio of the entire simulation, as reported by the SIMULINK Solver Profiler, was 7.5 for our approach and 12.15 for the original approach. This result highlights a computational improvement of approximately 38%, demonstrating the efficiency of the proposed method.

VII. CONCLUSION

In this work, an impact-resilient control method is proposed to achieve high accuracy in path tracking during free motion and to reduce damage from unexpected impacts for a generic 6-DoF HHM. In addition, a novel representation of the GMO is introduced in Plücker coordinates for the first time, aligning with the dynamics of the proposed scheme. The stability of the system under the new control command is proved using the VPF and the virtual stability concepts of VDC. Extensive experiments have been conducted to evaluate the performance of the proposed scheme. The results show that the designed impact-resilient approach achieves subcentimeter tracking accuracy and reduces the impact of contact by 80%.

For future work, we aim to address certain limitations of this study and extend our approach toward a more general control solution. Currently, the approach assumes contact occurs only at the end-effector, and a first-order impedance model is used. While these assumptions align well with many real-world

applications, addressing them will be essential to create a more versatile solution suitable for unstructured environments.

APPENDIX

A. Derivative of Inertia Matrix

Spatial inertia matrix in (5) is a symmetric dyadic tensor that maps \mathcal{M}^6 to \mathcal{F}^6 . Consequently, it can be expressed as the sum of six symmetric dyads as [30]

$$M_A = \sum_{i=1}^6 \mathbf{m}_i \mathbf{m}_i \bullet \quad \mathbf{m}_i \in \mathcal{F}^6 \quad (47)$$

with $\mathbf{m}_i \bullet = \mathbf{m}_i^T$. It must be mention that M_A is fixed to the body and only varies with the body motion, allowing to represent it as a sum of dyads in which each of \mathbf{m}_i is all fixed to the corresponding body. Consequently, we can define \times operator for 6-D vectors as $\dot{\mathbf{m}}_i = {}^A\mathcal{V} \times^* \mathbf{m}_i$ with ${}^A\mathcal{V} \times^* = -({}^A\mathcal{V} \times)^T$, and

$${}^A\mathcal{V} \times = \begin{bmatrix} {}^A\omega \times & {}^A\mathcal{V} \times \\ 0 & {}^A\omega \times \end{bmatrix}, \quad \alpha \times = \begin{bmatrix} 0 & -\alpha_z & \alpha_y \\ \alpha_z & 0 & -\alpha_x \\ -\alpha_y & \alpha_x & 0 \end{bmatrix} \quad (48)$$

where $\alpha = [\alpha_x, \alpha_y, \alpha_z] \in R^3$ is any vector. Then, the derivative of M_A can be computed as follows:

$$\begin{aligned} \frac{d}{dt} M_A &= \sum_{i=1}^6 \dot{\mathbf{m}}_i \mathbf{m}_i \bullet + \mathbf{m}_i \dot{\mathbf{m}}_i \bullet \\ &= \sum_{i=1}^6 ({}^A\mathcal{V} \times^* \mathbf{m}_i) \mathbf{m}_i \bullet + \sum_{i=1}^6 \mathbf{m}_i ({}^A\mathcal{V} \times^* \mathbf{m}_i) \bullet \\ &= {}^A\mathcal{V} \times^* \sum_{i=1}^6 \mathbf{m}_i \mathbf{m}_i \bullet - \left(\sum_{i=1}^6 \mathbf{m}_i \mathbf{m}_i \bullet \right) {}^A\mathcal{V} \times \\ &= -({}^A\mathcal{V} \times)^T M_A - M_A {}^A\mathcal{V} \times. \end{aligned} \quad (49)$$

B. Lemma 1

By recalling Definition (1), (28), (29), (34), (36), (39), (41), and $N_c^T N_c = I_6$, one can obtain

$$\begin{aligned} p_T &= ({}^T V_r - {}^T V)^T ({}^T F_r - {}^T F) \\ &= ((\dot{\mathcal{X}}_d - \dot{\mathcal{X}}) + \Gamma (\mathcal{X}_d - \mathcal{X}) + \Sigma (f_{ed} - \tilde{f}_e))^T (f_{ed} - f_e) \\ &= -(\dot{\mathcal{X}}_d - \dot{\mathcal{X}})^T (D_d \Sigma D_d - D_d) (\dot{\mathcal{X}}_d - \dot{\mathcal{X}}) \\ &\quad + (\mathcal{X}_d - \mathcal{X})^T (K_d \Sigma K_d - \Gamma K_d) (\mathcal{X}_d - \mathcal{X}) \\ &\quad + (\mathcal{X}_d - \mathcal{X})^T (2D_d \Sigma K_d - \Gamma D_d - K_d) (\dot{\mathcal{X}}_r - \dot{\mathcal{X}}). \end{aligned} \quad (50)$$

It can be seen from (50) that selecting the Γ and Σ as is in (31) and (32), respectively, yields in $p_T = 0$.

C. Proof of Theorem 3

Consider the accompanying function for the system with tool body excluded as ν_R with its time derivative as

$$\dot{\nu}_R \leq -\bar{\alpha}_1 \nu_R + \bar{\alpha}_0 - p_{E_4} \quad (51)$$

with p_{E_4} being VPF at the driven cutting point [see Fig. 2(c)]. Let $\nu_T = \nu_1 + \nu_R$ be the accompanying function of the entire system. Then, using (45) and (51) along with Lemma 2 with following the same procedure in [25], one can achieve:

$$\dot{\nu}_T \leq -\mu \nu_T + \mu_0 \quad (52)$$

which ensures the SGUUB for entire system in the sense of Theorem 1.

REFERENCES

- [1] J. Mattila, J. Koivumäki, D. G. Caldwell, and C. Semini, "A survey on control of hydraulic robotic manipulators with projection to future trends," *IEEE/ASME Trans. Mechatron.*, vol. 22, no. 2, pp. 669–680, Apr. 2017.
- [2] M. Cheng, L. Li, R. Ding, B. Xu, P. Jiang, and J. Mattila, "Prioritized multitask flow optimization of redundant hydraulic manipulator," *IEEE/ASME Trans. Mechatron.*, vol. 29, no. 1, pp. 487–498, Feb. 2024.
- [3] J. Yao, Z. Jiao, D. Ma, and L. Yan, "High-accuracy tracking control of hydraulic rotary actuators with modeling uncertainties," *IEEE/ASME Trans. Mechatron.*, vol. 19, no. 2, pp. 633–641, Apr. 2014.
- [4] D. Jud et al., "HEAP-the autonomous walking excavator," *Autom. Construction*, vol. 129, 2021, Art. no. 103783.
- [5] Z. Xu, W. Deng, H. Shen, and J. Yao, "Extended-state-observer-based adaptive prescribed performance control for hydraulic systems with full-state constraints," *IEEE/ASME Trans. Mechatron.*, vol. 27, no. 6, pp. 5615–5625, Dec. 2022.
- [6] A. Mohanty and B. Yao, "Integrated direct/indirect adaptive robust control of hydraulic manipulators with valve deadband," *IEEE/ASME Trans. Mechatron.*, vol. 16, no. 4, pp. 707–715, Aug. 2011.
- [7] H. V. A. Truong, S. Nam, S. Kim, Y. Kim, and W. K. Chung, "Backstepping-sliding-mode-based neural network control for electro-hydraulic actuator subject to completely unknown system dynamics," *IEEE Trans. Autom. Sci. Eng.*, vol. 21, no. 4, pp. 6202–6216, Oct. 2024.
- [8] T. Mononen, M. M. Aref, and J. Mattila, "Nonlinear model predictive control of a heavy-duty hydraulic bulldozer blade," in *Proc. IEEE Int. Conf. Cybern. Intell. Syst. IEEE Conf. Robot. Automat. Mechatron.*, 2019, pp. 565–570.
- [9] Z. Yao, F. Xu, G.-P. Jiang, and J. Yao, "Data-driven control of hydraulic manipulators by reinforcement learning," *IEEE/ASME Trans. Mechatron.*, vol. 29, no. 4, pp. 2673–2684, Aug. 2024.
- [10] X. Liang, Z. Yao, W. Deng, and J. Yao, "Adaptive neural network finite-time tracking control for uncertain hydraulic manipulators," *IEEE/ASME Trans. Mechatron.*, vol. 30, no. 1, pp. 645–656, Feb. 2025.
- [11] W.-H. Zhu, *Virtual Decomposition Control: Toward Hyper Degrees of Freedom Robots*, vol. 60. Berlin, Germany: Springer, 2010.
- [12] J. Koivumäki and J. Mattila, "High performance nonlinear motion/force controller design for redundant hydraulic construction crane automation," *Autom. Construction*, vol. 51, pp. 59–77, 2015.
- [13] J. Koivumäki, W.-H. Zhu, and J. Mattila, "Energy-efficient and high-precision control of hydraulic robots," *Control Eng. Pract.*, vol. 85, pp. 176–193, 2019.
- [14] B. Zhou, F. Gao, J. Pan, and S. Shen, "Robust real-time UAV replanning using guided gradient-based optimization and topological paths," in *Proc. IEEE Int. Conf. Robot. Automat.*, 2020, pp. 1208–1214.
- [15] J. A. Preiss, K. Hausman, G. S. Sukhatme, and S. Weiss, "Trajectory optimization for self-calibration and navigation," in *Proc. Robot.: Sci. Syst.*, vol. 13, 2017.
- [16] Z. Lu, Z. Liu, M. Campbell, and K. Karydis, "Online search-based collision-inclusive motion planning and control for impact-resilient mobile robots," *IEEE Trans. Robot.*, vol. 39, no. 2, pp. 1029–1049, Apr. 2023.
- [17] Z. Lu, Z. Liu, and K. Karydis, "Deformation recovery control and post-impact trajectory replanning for collision-resilient mobile robots," in *Proc. IEEE/RSJ Int. Conf. Intell. Robots Syst.*, 2021, pp. 2030–2037.
- [18] Q. Ha, Q. Nguyen, D. Rye, and H. Durrant-Whyte, "Impedance control of a hydraulically actuated robotic excavator," *Autom. Construction*, vol. 9, no. 5/6, pp. 421–435, 2000.
- [19] T. Qin, Y. Li, L. Quan, and L. Yang, "An adaptive robust impedance control considering energy-saving of hydraulic excavator boom and stick systems," *IEEE/ASME Trans. Mechatron.*, vol. 27, no. 4, pp. 1928–1936, Aug. 2022.
- [20] J. Koivumäki and J. Mattila, "Stability-guaranteed force-sensorless contact force/motion control of heavy-duty hydraulic manipulators," *IEEE Trans. Robot.*, vol. 31, no. 4, pp. 918–935, Aug. 2015.

- [21] H. Feng, Q. Song, C. Yin, and D. Cao, "Adaptive impedance control method for dynamic contact force tracking of robotic excavators," *J. Construction Eng. Manage.*, vol. 148, no. 11, 2022, Art. no. 04022124.
- [22] J. Koivumäki and J. Mattila, "Stability-guaranteed impedance control of hydraulic robotic manipulators," *IEEE/ASME Trans. Mechatron.*, vol. 22, no. 2, pp. 601–612, Apr. 2017.
- [23] S. Yoo, W. Lee, and W. K. Chung, "Impedance control of hydraulic actuation systems with inherent backdrivability," *IEEE/ASME Trans. Mechatron.*, vol. 24, no. 5, pp. 1921–1930, Oct. 2019.
- [24] R.-q. Ding, J.-h. Wang, M. Cheng, M.-k. Sun, B. Xu, and Z. Wang, "Adaptive impedance control for the hydraulic manipulator under the uncertain environment," *J. Braz. Soc. Mech. Sci. Eng.*, vol. 45, no. 8, 2023, Art. no. 437.
- [25] M. Hejrati and J. Mattila, "Orchestrated robust controller for precision control of heavy-duty hydraulic," *IEEE Trans. Automat. Sci. Eng.*, early access, Apr. 10, 2025, doi: [10.1109/TASE.2025.3559595](https://doi.org/10.1109/TASE.2025.3559595).
- [26] A. D. Luca, A. Albu-Schaffer, S. Haddadin, and G. Hirzinger, "Collision detection and safe reaction with the DLR-III lightweight manipulator arm," in *Proc. IEEE/RSJ Int. Conf. Intell. Robots Syst.*, 2006, pp. 1623–1630.
- [27] S. Lampinen, J. Koivumäki, W.-H. Zhu, and J. Mattila, "Force-sensor-less bilateral teleoperation control of dissimilar master–slave system with arbitrary scaling," *IEEE Trans. Control Syst. Technol.*, vol. 30, no. 3, pp. 1037–1051, May 2022.
- [28] L. Ding, H. Xing, H. Gao, A. Torabi, W. Li, and M. Tavakoli, "VDC-based admittance control of multi-DoF manipulators considering joint flexibility via hierarchical control framework," *Control Eng. Pract.*, vol. 124, 2022, Art. no. 105186.
- [29] M. Hejrati and J. Mattila, "Nonlinear subsystem-based adaptive impedance control of physical human-robot-environment interaction in contact-rich tasks," *IEEE Trans. Robot. Autom.*, vol. 8, no. 10, pp. 6083–6090, Oct. 2023.
- [30] R. Featherstone, *Rigid Body Dynamics Algorithms*. Berlin, Germany: Springer, 2014.
- [31] M. Hejrati and J. Mattila, "Decentralized nonlinear control of redundant upper limb exoskeleton with natural adaptation law," in *Proc. IEEE-RAS 21st Int. Conf. Humanoid Robots*, 2022, pp. 269–276.
- [32] T. Lee, J. Kwon, and F. C. Park, "A natural adaptive control law for robot manipulators," in *Proc. IEEE/RSJ Int. Conf. Intell. Robots Syst.*, 2018, pp. 1–9.
- [33] M. Hejrati and J. Mattila, "Physical human–robot interaction control of an upper limb exoskeleton with a decentralized neuroadaptive control scheme," *IEEE Trans. Control Syst. Technol.*, vol. 32, no. 3, pp. 905–918, May 2024.
- [34] W.-H. Zhu, Y.-G. Xi, Z.-J. Zhang, Z. Bien, and J. D. Schutter, "Virtual decomposition based control for generalized high dimensional robotic systems with complicated structure," *IEEE Trans. Robot. Autom.*, vol. 13, no. 3, pp. 411–436, Jun. 1997.



Mahdi Hejrati received the M.Sc. degree in mechanical engineering from the Sharif University of Technology, Tehran, Iran, in 2021. He is currently working toward the Ph.D. degree in automation engineering with the unit of Automation Technology and Mechanical Engineering, Tampere University, Tampere, Finland.

His research interests include nonlinear model-based control, physical human–robot interaction, and human-inspired control.



Jouni Mattila received the M.Sc. (Eng.) degree and the Dr. Tech. degree in automation engineering from the Tampere University of Technology, Tampere, Finland, in 1995 and 2000, respectively.

He is currently a Professor of machine automation with the unit of Automation Technology and Mechanical Engineering, Tampere University, Tampere. His research interests include machine automation, nonlinear model-based control of robotic manipulators, and energy-efficient control of heavy-duty mobile manipulators.